7340 *Inorg. Chem.* **2010**, *49*, 7340–7352
DOI: 10.1021/ic100325c

Inorganic Chemistry
Article

Unsymmetric Ru(II) Complexes with *N*-Heterocyclic Carbene and/or Terpyridine Ligands: Synthesis, Characterization, Ground- and Excited-State Electronic Structures and Their Application for DSSC Sensitizers

Hee-Jun Park,[†] Kyeong Ha Kim,[‡] Soo Young Choi,[†] Hyeong-Mook Kim,[†] Wan In Lee,[‡] Youn K. Kang,*[,§] and Young Keun Chung*[,†]

[†]*Intelligent Textile System Research Center, Department of Chemistry, College of Natural Sciences, Seoul National University, Seoul 151-747, Korea,* [‡]*Department of Chemistry, Inha University, Incheon, 402-751, Korea, and* [§]*Division of Chemistry and Molecular Engineering, Department of Chemistry, College of Natural Sciences, Seoul National University, Seoul 151-747, Korea*

Received February 18, 2010

Three ruthenium(II) complexes with *N*-heterocyclic carbene (NHC) or NHC/2,2′:6′,2″-terpyridine (tpy) hybrid ligands, bis[2,6-bis(3-methylimidazol-3-ium-1-yl)pyridine-4-carboxylic acid]ruthenium(II) (**BCN**), [2,6-bis(3-methylimidazolium-1-yl)pyridine-4-carboxylic acid](2,2′;6′2″-terpyridine)ruthenium(II) (**TCN**), and [2,6-bis(3-methylimidazol-3-ium-1-yl)pyridine](2,2′;6′2″-terpyridine-4′-carboxylic acid)ruthenium(II) (**CTN**), have been synthesized and characterized by ^{1}H and ^{13}C NMR, high-resolution mass spectrometry, and elemental analysis. The molecular geometry of the **TCN** complex was determined by X-ray crystallography. Electronic absorption spectra of these complexes exhibit typical $\pi-\pi^*$ and metal-to-ligand charge transfer bands in the UV and visible regions, respectively. The lowest energy absorption maxima were 430, 448, and 463 nm with molar extinction coefficients of 28 100, 15 400, and 7400 M^{-1}cm^{-1} for **BCN**, **TCN**, and **CTN**, respectively. Voltammetric data suggest that energy levels of the highest occupied molecular orbitals (HOMOs) of the three complexes reside within a 10 meV window despite the varying degrees of electronic effect of the constituent ligands. The electronic structures of these complexes calculated via density functional theory (DFT) indicate that the three HOMOs and the three lowest unoccupied MOs (LUMOs) are metal and ligand centered in character, for the former and the latter, respectively. Time-dependent DFT (TD-DFT) calculation predicts that the lowest energy absorption bands of each complex are comprised of multiple one-electron excitations. TD-DFT calculation also suggests that the background of spectral red shift stems most likely from the stabilization of unoccupied MOs rather than the destabilization of occupied MOs. The overall efficiencies of the dye-sensitized solar cell systems of these complexes were found to be 0.48, 0.14, and 0.10% for **BCN**, **TCN**, and **CTN**, respectively, while that of a commercial bis(4,4′-dicarboxylato-2,2′-bipyridine)-bis(isothiocyanoto)ruthenium(II) (N719) system was 6.34%.

Introduction

A plethora of ruthenium polypyridyl complexes have been extensively studied mainly due to their photophysical and electrochemical properties.[1−22] In particular, their robustness toward photooxidation has made them suitable not only for fundamental photochemical and photophysical studies

---

*To whom correspondence should be addressed. Telephone: (+82)-2-880-4390 (Y.K.K.), (+82)-2-880-6662 (Y.K.C.). Fax: (+82)-2-889-0310 (Y.K.K.), (+82)-2-889-0310 (Y.K.C.). E-mail: younkang@snu.ac.kr (Y.K.K.), ykchung@snu.ac.kr (Y.K.C.).

(1) *Photochemistry of Polypyridine and Porphyrin Complexes*; Kalyanasundaram, K., Ed.; Academic Press: London, 1992.

(2) Juris, A.; Balzani, V.; Barigelletti, F.; Campagna, S.; Belser, P.; Vonzelewsky, A. *Coord. Chem. Rev.* **1988**, *84*, 85–277.

(3) Sauvage, J. P.; Collin, J. P.; Chambron, J. C.; Guillerez, S.; Coudret, C.; Balzani, V.; Barigelletti, F.; Decola, L.; Flamigni, L. *Chem. Rev.* **1994**, *94*, 993–1019.

(4) Creutz, C.; Chou, M.; Netzel, T. L.; Okumura, M.; Sutin, N. *J. Am. Chem. Soc.* **1980**, *102*, 1309–1319.

(5) Rubinstein, I.; Bard, A. J. *J. Am. Chem. Soc.* **1980**, *102*, 6641–6642.

(6) Durham, B.; Caspar, J. V.; Nagle, J. K.; Meyer, T. J. *J. Am. Chem. Soc.* **1982**, *104*, 4803–4810.

(7) Constable, E. C.; Thompson, A.; Tocher, D. A.; Daniels, M. A. M. *New J. Chem.* **1992**, *16*, 855–867.

(8) Jenkins, Y.; Friedman, A. E.; Turro, N. J.; Barton, J. K. *Biochemistry* **1992**, *31*, 10809–10816.

(9) Vandiemen, J. H.; Hage, R.; Haasnoot, J. G.; Lempers, H. E. B.; Reedijk, J.; Vos, J. G.; Decola, L.; Barigelletti, F.; Balzani, V. *Inorg. Chem.* **1992**, *31*, 3518–3522.

(10) Kim, Y. I.; Atherton, S. J.; Brigham, E. S.; Mallouk, T. E. *J. Phys. Chem.* **1993**, *97*, 11802–11810.

(11) Argazzi, R.; Bignozzi, C. A.; Heimer, T. A.; Castellano, F. N.; Meyer, G. J. *Inorg. Chem.* **1994**, *33*, 5741–5749.

(12) Benniston, A. C.; Grosshenny, V.; Harriman, A.; Ziessel, R. *Angew. Chem., Int. Ed.* **1994**, *33*, 1884–1885.

(13) Balzani, V.; Juris, A.; Venturi, M.; Campagna, S.; Serroni, S. *Chem. Rev.* **1996**, *96*, 759–833.

(14) Damrauer, N. H.; Cerullo, G.; Yeh, A.; Boussie, T. R.; Shank, C. V.; McCusker, J. K. *Science* **1997**, *275*, 54–57.

Published on Web 07/20/2010 © 2010 American Chemical Society

but also for applications that include artificial solar energy conversion devices.[23−31] The current understanding about the electronic structures of these types of coordination compounds have reached the level that the energetics of the electronic excited state can be manipulated to some extent. One of the most popular approaches is a design of the ligand with varying degrees of electronic effect so that the highest occupied molecular orbital−lowest unoccupied MO (HOMO−LUMO) gap as well as the absolute energy levels of the electronically excited states can be modulated. Besides the vast majority of polypyridyl compounds, common ligands in this class include heteroaromatic N,[32−34] C,[35−41] or S[42,43] donor molecules.

Recently, *N*-heterocyclic carbene (NHC) compounds have emerged as an important ligand in organometallic and inorganic chemistry due to their unique electronic and structural properties.[44−48] However, despite intense interest in the catalytic properties of transition-metal complexes with NHC ligands, reports on the study of their photophysical properties are limited.[22,49] We have previously reported the synthesis and photoluminescence properties of ruthenium NHC complexes in which 2-(3-methylimidazolium-1-yl)pyridine (mip) or 2,6-bis-(3-methylimidazolium-1-yl)pyridine (bip) was utilized as a bi- or tridentate ligand to the ruthenium(II) ion forming a new type of ruthenium chromophore.[22] Being both mip and bip topological analogues of 2,2′-bipyridine (bpy) and 2,2′;6′2″-terpyridine (tpy), respectively, the structures of $[Ru(mip)_3]^{2+}$ and $[Ru(bip)_2]^{2+}$ complexes are quite similar to those of $[Ru(bpy)_3]^{2+}$ and $[Ru(tpy)_2]^{2+}$, respectively. These complexes exhibit their lowest energy absorption maxima at ∼380 nm with extinction coefficients similar to that of $[Ru(bpy)_3]^{2+}$ (15 200−20 100 $M^{-1}cm^{-1}$ depending on the counteranion). Due to the higher electron-donating effect of NHC ligands relative to polypyridyl ones,[48,50−53] the first oxidation potential of such complexes were ca. 1.38 V vs NHE, which was ca. 0.2 V more negative than that of the ruthenium polypyridyl counterpart. The triplet state lifetime ranged 490−3100 ns depending on the counteranions and solvents, which is similar to that of $[Ru(bpy)_3]^{2+}$ (860 ns) but is definitely longer than that of $[Ru(tpy)_2]^{2+}$ (0.25 ns). These features, combined with the previously reported thermal stabilities of transition-metal carbene complexes,[54−56] strongly suggest a use for these types of complexes as photosensitizers of dye-sensitized solar cells (DSSC). It is well-known, however, that a large part of the solar spectrum reaching the terrestrial surface resides in the visible-to-near IR region. To fully take advantage of solar spectrum, it is a prerequisite to drive the absorption bands of ruthenium NHC complexes, currently focused in the UV region, toward longer wavelength ones.

In the ruthenium complexes where the lowest electronic transition is an metal-to-ligand charge transfer (MLCT),[1] the common approach to shift an absorption band to the lower energy region is either lowering the energy of the ligand-based LUMO or raising that of the metal-based HOMO. Both the experimental voltammetric data and the theoretical calculation results indicate that the metal-based HOMO levels of ruthenium NHC complexes are higher than those of ruthenium polypyridyl counterparts due to the stronger

---

(15) Kalyanasundaram, K.; Gratzel, M. *Coord. Chem. Rev.* **1998**, *177*, 347–414.

(16) Nazeeruddin, M. K.; Zakeeruddin, S. M.; Humphry-Baker, R.; Jirousek, M.; Liska, P.; Vlachopoulos, N.; Shklover, V.; Fischer, C. H.; Gratzel, M. *Inorg. Chem.* **1999**, *38*, 6298–6305.

(17) Vogtle, F.; Plevoets, M.; Nieger, M.; Azzellini, G. C.; Credi, A.; De Cola, L.; De Marchis, V.; Venturi, M.; Balzani, V. *J. Am. Chem. Soc.* **1999**, *121*, 6290–6298.

(18) Barigelletti, F.; Flamigni, L. *Chem. Soc. Rev.* **2000**, *29*, 1–12.

(19) Bignozzi, C. A.; Argazzi, R.; Kleverlaan, C. J. *Chem. Soc. Rev.* **2000**, *29*, 87–96.

(20) Uyeda, H. T.; Zhao, Y. X.; Wostyn, K.; Asselberghs, I.; Clays, K.; Persoons, A.; Therien, M. J. *J. Am. Chem. Soc.* **2002**, *124*, 13806–13813.

(21) Baranoff, E.; Collin, J. P.; Flamigni, L.; Sauvage, J. P. *Chem. Soc. Rev.* **2004**, *33*, 147–155.

(22) Son, S. U.; Park, K. H.; Lee, Y. S.; Kim, B. Y.; Choi, C. H.; Lah, M. S.; Jang, Y. H.; Jang, D. J.; Chung, Y. K. *Inorg. Chem.* **2004**, *43*, 6896–6898.

(23) Amadelli, R.; Argazzi, R.; Bignozzi, C. A.; Scandola, F. *J. Am. Chem. Soc.* **1990**, *112*, 7099–7103.

(24) Oregan, B.; Gratzel, M. *Nature* **1991**, *353*, 737–740.

(25) Nazeeruddin, M. K.; Pechy, P.; Renouard, T.; Zakeeruddin, S. M.; Humphry-Baker, R.; Comte, P.; Liska, P.; Cevey, L.; Costa, E.; Shklover, V.; Spiccia, L.; Deacon, G. B.; Bignozzi, C. A.; Gratzel, M. *J. Am. Chem. Soc.* **2001**, *123*, 1613–1624.

(26) Hara, K.; Sugihara, H.; Tachibana, Y.; Islam, A.; Yanagida, M.; Sayama, K.; Arakawa, H.; Fujihashi, G.; Horiguchi, T.; Kinoshita, T. *Langmuir* **2001**, *17*, 5992–5999.

(27) Kuciauskas, D.; Freund, M. S.; Gray, H. B.; Winkler, J. R.; Lewis, N. S. *J. Phys. Chem. B* **2001**, *105*, 392–403.

(28) Wang, P.; Zakeeruddin, S. M.; Moser, J. E.; Nazeeruddin, M. K.; Sekiguchi, T.; Gratzel, M. *Nat. Mater.* **2003**, *2*, 402–407.

(29) Alstrum-Acevedo, J. H.; Brennaman, M. K.; Meyer, T. J. *Inorg. Chem.* **2005**, *44*, 6802–6827.

(30) Anderson, N. A.; Lian, T. Q. *Annu. Rev. Phys. Chem.* **2005**, *56*, 491–519.

(31) Wang, Z. S.; Hara, K.; Dan-Oh, Y.; Kasada, C.; Shinpo, A.; Suga, S.; Arakawa, H.; Sugihara, H. *J. Phys. Chem. B* **2005**, *109*, 3907–3914.

(32) Wu, P. C.; Yu, J. K.; Song, Y. H.; Chi, Y.; Chou, P. T.; Peng, S. M.; Lee, G. H. *Organometallics* **2003**, *22*, 4938–4946.

(33) Tung, Y. L.; Lee, S. W.; Chi, Y.; Chen, L. S.; Shu, C. F.; Wu, F. I.; Carty, A. J.; Chou, P. T.; Peng, S. M.; Lee, G. M. *Adv. Mater.* **2005**, *17*, 1059–1064.

(34) Chou, P. T.; Chi, Y. *Chem.—Eur. J.* **2007**, *13*, 380–395.

(35) Reveco, P.; Schmehl, R. H.; Cherry, W. R.; Fronczek, F. R.; Selbin, J. *Inorg. Chem.* **1985**, *24*, 4078–4082.

(36) Constable, E. C.; Holmes, J. M. *J. Organomet. Chem.* **1986**, *301*, 203–208.

(37) Serroni, S.; Juris, A.; Campagna, S.; Venturi, M.; Denti, G.; Balzani, V. *J. Am. Chem. Soc.* **1994**, *116*, 9086–9091.

(38) Barigelletti, F.; Flamigni, L.; Guardigli, M.; Juris, A.; Beley, M.; ChodorowskiKimmes, S.; Collin, J. P.; Sauvage, J. P. *Inorg. Chem.* **1996**, *35*, 136–142.

(39) Fraysse, S.; Coudret, C.; Launay, J. P. *J. Am. Chem. Soc.* **2003**, *125*, 5880–5888.

(40) Dragutan, V.; Dragutan, I.; Delaude, L.; Demonceau, A. *Coord. Chem. Rev.* **2007**, *251*, 765–794.

(41) Wadman, S. H.; Lutz, M.; Tooke, D. M.; Spek, A. L.; Hartl, F.; Havenith, R. W. A.; van Klink, G. P. M.; van Koten, G. *Inorg. Chem.* **2009**, *48*, 1887–1900.

(42) Constable, E. C.; Sousa, L. R. *J. Organomet. Chem.* **1992**, *427*, 125–139.

(43) Constable, E. C.; Dunne, S. J.; Rees, D. G. F.; Schmitt, C. X. *Chem. Commun.* **1996**, 1169–1170.

(44) Herrmann, W. A. *Angew. Chem., Int. Ed.* **2002**, *41*, 1290–1309.

(45) Enders, D.; Balensiefer, T. *Acc. Chem. Res.* **2004**, *37*, 534–541.

(46) Crudden, C. M.; Allen, D. P. *Coord. Chem. Rev.* **2004**, *248*, 2247–2273.

(47) Khramov, D. M.; Lynch, V. M.; Bielawski, C. W. *Organometallics* **2007**, *26*, 6042–6049.

(48) de Fremont, P.; Marion, N.; Nolan, S. P. *Coord. Chem. Rev.* **2009**, *253*, 862–892.

(49) Poyatos, M.; Mata, J. A.; Falomir, E.; Crabtree, R. H.; Peris, E. *Organometallics* **2003**, *22*, 1110–1114.

(50) Heinemann, C.; Muller, T.; Apeloig, Y.; Schwarz, H. *J. Am. Chem. Soc.* **1996**, *118*, 2023–2038.

(51) Grundemann, S.; Albrecht, M.; Loch, J. A.; Faller, J. W.; Crabtree, R. H. *Organometallics* **2001**, *20*, 5485–5488.

(52) Herrmann, W. A.; Schutz, J.; Frey, G. D.; Herdtweck, E. *Organometallics* **2006**, *25*, 2437–24489.

(53) Jacobsen, H.; Correa, A.; Poater, A.; Costabile, C.; Cavallo, L. *Coord. Chem. Rev.* **2009**, *253*, 687–703.

(54) Huang, J. K.; Schanz, H. J.; Stevens, E. D.; Nolan, S. P. *Organometallics* **1999**, *18*, 5375–5380.

(55) Karimi, B.; Enders, D. *Org. Lett.* **2006**, *8*, 1237–1240.

(56) Clavier, H.; Nolan, S. P. *Chem.—Eur. J.* **2007**, *13*, 8029–8036.

electron-donating effect of the NHC ligands.[22] On the other hand, the energy difference between the LUMO of $[Ru(bip)_2]^{2+}$ and that of $[Ru(tpy)_2]^{2+}$ is even larger than that between their HOMOs, which gives rise to the increase of electronic transition energy of $[Ru(bip)_2]^{2+}$ relative to that of $[Ru(tpy)_2]^{2+}$. Thus our tentative strategy to reduce the HOMO−LUMO gap is simply substituting one bip ligand with a less electron-donating tpy one, anticipating that the LUMO level of the prepared complex would be lowered, while the HOMO level is maintained. Under this strategy we have synthesized three new complexes possessing bip or bip/tpy hybrid ligands. Herein we report our experimental and theoretical studies regarding the photo- and electrochemical properties of these complexes in relation to their DSSC performance.

Experimental Section

Materials. All reactions were carried out under a nitrogen atmosphere unless otherwise noted. Standard Schlenk techniques were employed to manipulate air-sensitive solutions, while workup procedures were done in air. All solvents utilized in this work were obtained from Fisher Scientific (HPLC grade) unless otherwise noted. Tetrahydrofuran (THF) and diethylether (Et_2O) were dried over Na/benzophenone and were subsequently distilled under nitrogen prior to use. Absolute methyl and ethyl alcohols, 1,2-ethanediol (Aldrich, 99%), acetone (HPLC grade), and triethylamine (Aldrich, 99.5%) were used without any further purification. Lithium hydroxide (LiOH), lithium iodide (LiI), 4-*tert*-butylpyridine (TBP), methoxyacetonitrile, and sodium hexafluorophosphate ($NaPF_6$) were purchased from Aldrich Chemical Co. and were used as received. 1-Hexyl-2,3-dimethyl-imidazolium iodide (HDMII) was purchased from Merck and was used as received. All deuterated solvents were purchased from Cambridge Isotope Laboratories, Inc. 2,6-Bis(3-methylimidazolium-1-yl)pyridine dibromide (**L2**)[57] and (2,2′:6′,2″-terpyridine)(trichloro)Ru(III) ($[(tpy)RuCl_3]$)[58] were prepared according to literature procedures. Chromatographic purification (Silica Gel 60, 230−400 mesh, Merck) of all compounds was performed on the benchtop.

Instrumentation. ^1H NMR spectra were recorded on a Bruker 300 spectrometer. Chemical shifts for ^1H NMR spectra are relative to a residual proton in the deuterated solvents ($CDCl_3$, $\delta = 7.24$ ppm). All coupling constants are reported in hertz. Elemental analyses were done at the National Center for Inter-University Research Facilities located in the Seoul National University. High-resolution mass spectrometry (HRMS) data were obtained at the Korea Basic Science Institute. Electronic absorption spectra were recorded on a Beckman Du-650 spectrophotometer. Cyclic voltammograms were obtained with a CH Instrument voltammetric analyzer. Measurements were performed by purging the acetonitrile (spectroscopic grade) solution by dry nitrogen gas for 30 min. The supporting electrolyte was 0.1 M tetrabultylammonium hexafluorophosphate ($TBAPF_6$). Glassy carbon and Ag/Ag^+ (0.01 M $AgNO_3$) were used as working and reference electrodes, respectively. The scan rate was maintained at 100 mV/s.

Synthesis of [(2,6-Bis(3-methylimidazolium-1-yl)pyridine-4-carboxylic acid)] dibromide (L1). In a 8 mL vial, 2,6-dibromopyridine-4-carboxylic acid[59] (0.35 g, 1.24 mmol) and 1-methylimidazole (1 mL, 12.4 mmol) were heated at 150 °C without solvent for 3 h. After the solution was cooled, Et_2O (5 mL) was added to the mixture, and the resultant precipitate was filtered. The crude product was dissolved in MeOH and was triturated in Et_2O to afford the product **L1** as a white solid. Yield: 0.39 g (0.87 mmol, 70%); ^1H NMR (300 MHz, DMSO-d_6): δ 10.49 (s, 2 H), 8.87 (s, 2 H), 8.50 (s, 2 H), 8.05 (s, 2 H), 4.02 (s, 6 H); ^{13}C NMR (75 MHz, DMSO-d_6): δ 164.38, 155.74, 145.89, 137.13, 125.21, 119.69, 113.87, 36.92; m/z (FABMS) 364.0412 $[M - Br]^+$ (theoretical value 364.0409).

Synthesis of $[(tpy\text{-}CO_2H)RuCl_3]$. A mixture of ruthenium(III) chloride (0.220 g, 0.84 mmol) and 2,2′:6′,2″-terpyridine-4′-carboxylic acid[59] (0.212 g, 0.76 mmol) in absolute ethanol (80 mL) was heated at reflux for 4 h. The reaction mixture was cooled to room temperature and was poured on the glass filter. The filtered brown powder was washed with absolute ethanol and Et_2O sequentially and dried in vacuo. Yield: 0.20 g (0.41 mmol, 54%); m/z (FABMS) 448.9270 $[M - Cl]^+$ (theoretical value 448.9272).

Synthesis of BCN. A mixture of **L1** (0.223 g, 0.50 mmol) and ruthenium(III) chloride (0.065 g, 0.25 mmol) in 7 mL of 1,2-ethanediol was heated at 180 °C for 4 h. After the solution was cooled, an aqueous solution of $NaPF_6$ (0.5 g, 3.0 mmol in 5 mL of water) was added to the reaction mixture. The resulting precipitates were filtered and dried. The solid was dissolved in 2 mL of THF, and an aqueous solution of LiOH (2.4 mg, 1.0 mmol in 4 mL of water) was added. After the solution was stirred for 30 min, THF was removed on a rotary evaporator, and the solution was cooled in an ice bath. The solution was acidified by slow addition of aqueous HCl (0.25 mL, 2 M). The orange solid was isolated by filtration. The crude product was purified by column chromatography on silica gel. Elution with acetone/MeOH/saturated $NaPF_6$ (49:49:2) gave **BCN** as orange band. The collected orange solution was concentrated to ca. 5 mL and was triturated in water. The precipitated orange solids were filtered, washed several times with water, and dried in vacuo. **BCN** was obtained as orange solids. Yield: 0.18 g (0.19 mmol, 77%); ^1H NMR (300 MHz, acetone-d_6): δ 8.65 (d, 2.0 Hz, 4 H), 8.61 (s, 4 H), 7.32 (d, 2.0 Hz, 4 H), 2.83 (s, 12 H); ^{13}C NMR (75 MHz, acetone-d_6): δ 189.38, 164.19, 151.78, 139.32, 124.79, 117.24, 105.91, 35.32; m/z (FABMS) 813.0828 $[M - PF_6]^+$ (theoretical value 813.0824). Anal. calcd for $C_{28}H_{26}N_{10}O_4RuP_2F_{12}$: C, 35.07; H, 2.74; N, 14.62. Found: C, 34.83; H, 2.75; N, 14.60.

Synthesis of TCN. A mixture of **L1** (0.045 g, 0.10 mmol) and $[(tpy)RuCl_3]$ (0.044 g, 0.10 mmol) in 3 mL of 1,2-ethanediol was heated at 180 °C for 3 h. After the solution was cooled, an aqueous solution of $NaPF_6$ (0.2 g, 1.2 mmol in 3 mL of water) was added to the reaction mixture. The resulting precipitates were filtered and dried. The solid was dissolved in 1 mL of THF, and an aqueous solution of LiOH (4.8 mg, 0.2 mmol in 2 mL of water) was added. After the solution was stirred for 30 min, THF was removed on the rotary evaporator, and the solution was cooled in an ice bath. The solution was acidified by slow addition of aqueous HCl (0.5 mL, 2 M). The orange solid was isolated by filtration. The crude product was purified by column chromatography on silica gel. Elution with acetone/MeOH/saturated $NaPF_6$ (49:49:2) followed by a trituration process, as described above, gave **TCN** as orange solids. Yield: 0.02 g (0.02 mmol, 21%); ^1H NMR (300 MHz, acetone-d_6): δ 9.10 (d, 8.1 Hz, 2 H), 8.88 (d, 8.0 Hz, 2 H), 8.80 (s, 2 H), 8.79 (s, 2 H), 8.59 (t, 8.1 Hz, 1 H), 8.17 (t, 7.7 Hz, 2 H), 7.80 (d, 5.3 Hz, 2 H), 7.40−7.36 (m, 4 H), 3.09 (s, 6 H); ^{13}C NMR (75 MHz, acetone-d_6): δ 189.20, 164.15, 156.74, 153.88, 153.57, 152.66, 141.63, 137.06, 134.29, 127.00, 124.91, 124.19, 123.48, 118.24, 106.97, 35.08; m/z (FABMS) 763.0715 $[M - PF_6]^+$ (theoretical value 763.0708). Anal. calcd for $C_{29}H_{24}N_8O_2RuP_2F_{12}$: C, 38.32; H, 2.66; N, 12.34. Found: C, 37.90; H, 2.84; N, 12.17.

Synthesis of Complex CTN. A mixture of **L2** (0.077 g, 0.19 mmol), $[(tpy\text{-}CO_2H)RuCl_3]$ (0.102 g, 0.21 mmol), and NEt_3 (0.117 g, 0.16 mL, 1.2 mmol) in 5 mL of EtOH and 1 mL of DMF was stirred at reflux for 12 h. After the solution was cooled, an aqueous solution of $NaPF_6$ (0.5 g, 3.0 mmol in 5 mL of water) was added to the reaction mixture. The resulting precipitates were filtered and dried. The crude solid was purified

---

(57) Inamoto, K.; Kuroda, J.; Hiroya, K.; Noda, Y.; Watanabe, M.; Sakamoto, T. *Organometallics* **2006**, *25*, 3095–3098.

(58) Winter, A.; Hummel, J.; Risch, N. *J. Org. Chem.* **2006**, *71*, 4862–4871.

(59) Fallahpour, R. A. *Synthesis* **2000**, 1138–1142.

Chart 1. Molecular Structures of Investigated Complexes **BCN**, **TCN**, and **CTN** Along with the Benchmarks $[Ru(bip)_2]^{2+}$ and $[Ru(tpy)_2]^{2+}$

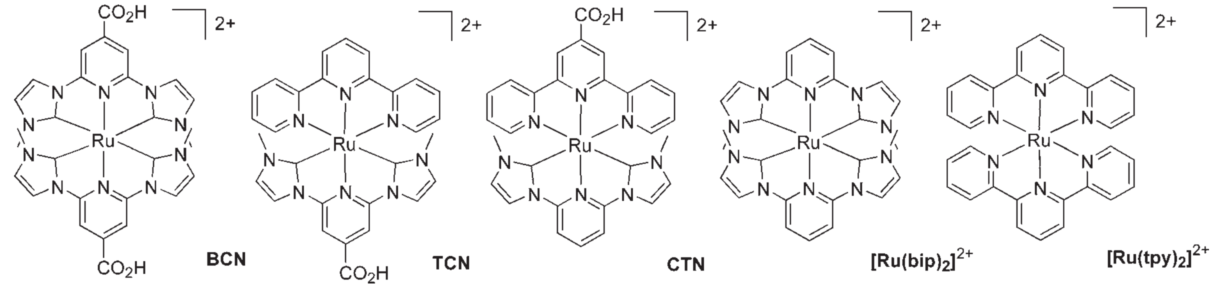

by column chromatography on silica gel. Elution with acetone/MeOH/saturated $NaPF_6$ (49:49:2) followed by trituration process as described above gave **CTN** as orange solids. Yield: 0.06 g (0.06 mmol, 33%); ^1H NMR (300 MHz, acetone-d_6): δ 9.29 (s, 2 H), 9.00 (d, 8.0 Hz, 2 H), 8.56 (t, 8.2 Hz, 1 H), 8.42 (d, 2.1 Hz, 2 H), 8.32 (d, 8.2 Hz, 2 H), 8.11 (t, 7.6 Hz, 2 H), 7.72 (d, 5.1 Hz, 2 H), 7.35 (t, 6.1 Hz, 2 H), 7.23 (d, 2.1 Hz, 2 H); ^{13}C NMR (75 MHz, acetone-d_6): δ 188.59, 164.67, 156.52, 154.48, 152.55, 152.47, 141.22, 136.99, 134.19, 127.36, 124.91, 124.62, 122.58, 118.02, 107.60, 35.28; *m*/*z* (FABMS) 763.0710 $[M - PF_6]^+$ (theoretical value 763.0708). Anal. calcd for $C_{29}H_{24}N_8O_2RuP_2F_{12}$: C, 38.32; H, 2.66; N, 12.34. Found: C, 37.75; H, 2.85; N, 12.13.

X-ray Structure of TCN. Single crystals of **TCN** suitable for the X-ray crystallography were grown by slow evaporation of acetonitrile and water solution (1:1) of **TCN** at room temperature. Diffraction data were collected on an Bruker SMART X-ray diffractometer at room temperature using graphite-monochromated Mo Kα radiation (λ = 0.71073 Å). The structures were solved by direct methods (SHELXS-97) and refined against all F^2 data (SHELX-97).[60,61] All nonhydrogen atoms were refined with anisotropic thermal parameters, and the hydrogen atoms were treated as idealized contributions.

Computational Method. All calculations were performed using the Gaussian 03 program package.[62] All the results were obtained using a spin-restricted formalism at the density functional theory (DFT) level of theory using the B3LYP hybrid functional.[63-65] The ruthenium atom was described by using the LANL2DZ basis set, which includes the relativistic effective core potential (ECP) of Hay and Wadt[66-68] for the inner electrons and the double-ζ basis set for the outer electrons. The standard 6-31G(d) basis set was used for the remaining atoms. All geometry optimization procedure was done without any symmetry restriction.

The excitation energies and oscillator strengths for the three complexes at the optimized geometry in the ground state are obtained by time-dependent (TD)-DFT calculations with the same basis sets as those for the ground state.[69,70] Solvent effects (acetonitrile) were taken into account by conductor-like polarizable continuum model (CPCM) implemented in the Gaussian 03 program package.

DSSC Fabrication and Characterization. For the preparation of the nanocrystalline TiO_2 electrode, the TiO_2 paste purchased from DyeSol Co. (TiO_2 paste DSL 18NR-T) was coated on a FTO glass (Pilkington, TEC-8, 8 Ω/sq) using a doctor-blade method. The coated film was baked at 150 °C for 30 min and subsequently calcined at 500 °C for 15 min. Finally, the thickness of the TiO_2 layer was determined to be $\sim$9 μm, according to the scanning electron microscopy (SEM) cross-sectional images of the fabricated TiO_2 films on the FTO layer (Supporting Information). For the dye adsorption, the TiO_2 film was immersed in 0.5 mM acetone solution of the sensitizing dyes for 24 h at room temperature.[71] It was then rinsed with acetone several times and dried under a stream of nitrogen gas. The Pt-coated FTO, used as a counter electrode, was prepared by dropping a 0.7 mM H_2PtCl_6 solution on a FTO glass followed by heating at 400 °C for 20 min in air. The electrolyte consisted of 0.7 M 1-butyl-3-methyl-imidazolium iodide (BMII, Merck Co.), 0.03 M I_2, 0.1 M guanidinium thiocyanate (GSCN, Aldrich Chemical Co.), 0.02 M LiI, and 0.5 M 4-*tert*-butylpyridine (TBP, Aldrich) in acetonitrile and valeronitrile (85:15 v/v). The active area of the dye-coated TiO_2 film was 0.420 cm^2.

Photocurrent-voltage measurements were performed using a Keithley model 2400 source measurement unit. A 300 W xenon lamp (Spectra-Physics) was used as the light source, and the light intensity was adjusted using an NREL-calibrated Si solar cell equipped with a KG-5 filter for approximating AM 1.5G one sun light intensity. The incident photon-to-current efficiency (IPCE) spectra were measured as a function of wavelength from 380 to 900 nm using a specially designed IPCE system (PV Measurements, Inc.) for DSSC. See Chart 1 for the investigated complexes.

Results and Discussions

Synthesis and Crystal Structure. The synthesis of three new complexes, **BCN**, **TCN**, and **CTN** is shown in Scheme 1. The **BCN** was prepared by a reaction between $RuCl_3$ and **L1** in a refluxing ethylene glycol solution. During the reaction, carboxylic acid groups were converted to 2-hydroxyethylesters

---

[60] Sheldrick, G. M. *Program for the Solution of Crystal Structure*; University of Göttingen: Göttingen, Germany, 1997.

[61] Sheldrick, G. M. *Program for Crystal Structure Refinement*; University of Göttingen: Göttinger, Germany, 1997.

[62] Frisch, M. J.; Trucks, G. W.; Schlegel, H. B.; Scuseria, G. E.; Robb, M. A.; Cheeseman, J. R.; Montgomery, J. A., Jr.; Vreven, T.; Kudin, K. N.; Burant, J. C.; Millam, J. M.; Iyengar, S. S.; Tomasi, J.; Barone, V.; Mennucci, B.; Cossi, M.; Scalmani, G.; Rega, N.; Petersson, G. A.; Nakatsuji, H.; Hada, M.; Ehara, M.; Toyota, K.; Fukuda, R.; Hasegawa, J.; Ishida, M.; Nakajima, T.; Honda, Y.; Kitao, O.; Nakai, H.; Klene, M.; Li, X.; Knox, J. E.; Hratchian, H. P.; Cross, J. B.; Bakken, V.; Adamo, C.; Jaramillo, J.; Gomperts, R.; Stratmann, R. E.; Yazyev, O.; Austin, A. J.; Cammi, R.; Pomelli, C.; Ochterski, J. W.; Ayala, P. Y.; Morokuma, K.; Voth, G. A.; Salvador, P.; Dannenberg, J. J.; Zakrzewski, V. G.; Dapprich, S.; Daniels, A. D.; Strain, M. C.; Farkas, O.; Malick, D. K.; Rabuck, A. D.; Raghavachari, K.; Foresman, J. B.; Ortiz, J. V.; Cui, Q.; Baboul, A. G.; Clifford, S.; Cioslowski, J.; Stefanov, B. B.; Liu, G.; Liashenko, A.; Piskorz, P.; Komaromi, I.; Martin, R. L.; Fox, D. J.; Keith, T.; Al-Laham, M. A.; Peng, C. Y.; Nanayakkara, A.; Challacombe, M.; Gill, P. M. W.; Johnson, B.; Chen, W.; Wong, M. W.; Gonzalez, C.; Pople, J. A. *Gaussian 03*, revision C.02; Gaussian, Inc.: Wallingford, CT, 2004.

[63] Lee, C. T.; Yang, W. T.; Parr, R. G. *Phys. Rev. B: Condens. Matter Mater. Phys.* **1988**, *37*, 785–789.

[64] Becke, A. D. *J. Chem. Phys.* **1993**, *98*, 5648–5652.

[65] Stephens, P. J.; Devlin, F. J.; Chabalowski, C. F.; Frisch, M. J. *J. Phys. Chem.* **1994**, *98*, 11623–11627.

[66] Hay, P. J.; Wadt, W. R. *J. Chem. Phys.* **1985**, *82*, 270–283.

[67] Wadt, W. R.; Hay, P. J. *J. Chem. Phys.* **1985**, *82*, 284–298.

[68] Hay, P. J.; Wadt, W. R. *J. Chem. Phys.* **1985**, *82*, 299–310.

[69] Runge, E.; Gross, E. K. U. *Phys. Rev. Lett.* **1984**, *52*, 997–1000.

[70] Bartolotti, L. J. *Phys. Rev. A: At., Mol., Opt. Phys.* **1982**, *26*, 2243–2244.

[71] For the adsorption of N719, ethanol was used instead of acetone.

Scheme 1. Synthesis of New Complexes

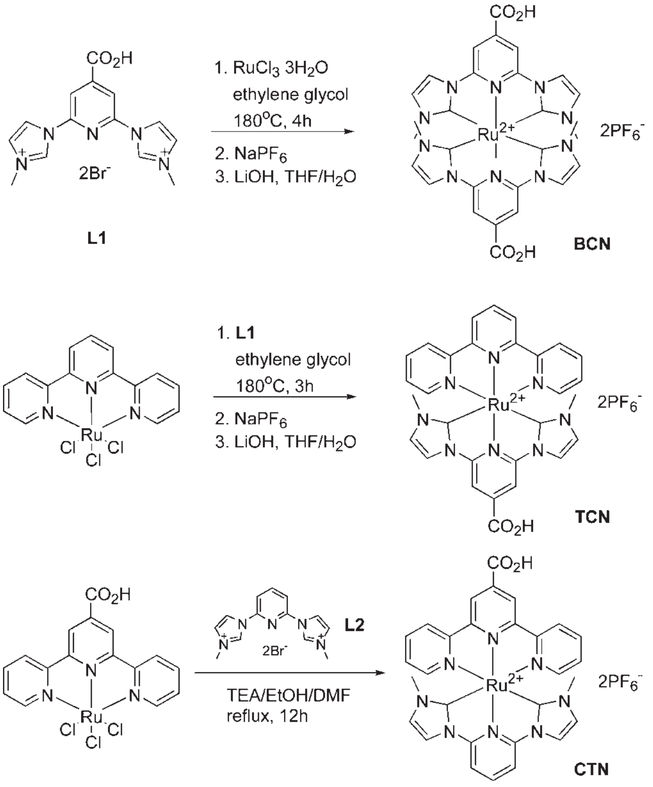

by the nucleophilic attack of ethylene glycol molecules.[72] A subsequent saponification with LiOH in THF/H_2O mixture gave **BCN**. The overall yield from these procedures was 77%. For the synthesis of **TCN**, we employed [Ru(tpy)Cl_3] as a starting material. The reaction between [Ru(tpy)Cl_3] and **L1** in refluxing ethylene glycol followed by saponification with LiOH in THF/H_2O mixture provided the desired complex in 21% yield. In the synthesis of **CTN**, however, a synthetic approach similar to that of **TCN** was not successful. Thus we adopt the method reported by Peris et al. in which triethylamine (TEA) was used as a base in a refluxing ethanol/DMF mixture.[49] The target complex **CTN** was produced in 33% yield.

The geometry of **TCN** complex has been determined by X-ray crystallography. The molecular formula of the obtained crystal structure of **TCN** was found to be [{2,6-bis-(3-methylimidazolium-1-yl)pyridine-4-carboxylate}(2,2′;6′2′′-terpyridine)ruthenium(II)]$PF_6^-\cdot 4H_2O$ due to the spontaneous deprotonation of carboxylic acid during the crystal growing (Figure 1). As a result, two C−O distances of carboxylate group were virtually identical (1.243 and 1.245 Å), and only one PF_6^- counteranion with some extent of disorder was associated in the crystal structure. The structure displays a typical geometry with both ligands coordinated in a tridentate, meridional fashion to the ruthenium(II) ion. The bond distances between the ruthenium ion and the six coordinated nitrogen or carbon atoms are very similar to those of $[Ru(tpy)_2]^{2+}$ and $[Ru(bip)_2]^{2+}$. For example, the central nitrogen-to-ruthenium bond distance of tpy ligand is 1.969 Å, which is very close to the mean distance of $[Ru(tpy)_2]^{2+}$ (1.976 ± 0.018 Å).[41] Interestingly, however, the central nitrogen-to-ruthenium bond distance of bip-CO_2^- ligand is 2.026 Å, which is even longer than that of $[Ru(bip)_2]^{2+}$(2.0177 and 2.0198 Å).[22] The slight increase of this bond length is probably due to the anionic carboxylate substituent, which actually acts as a mild electron-donating group upon deprotonation.

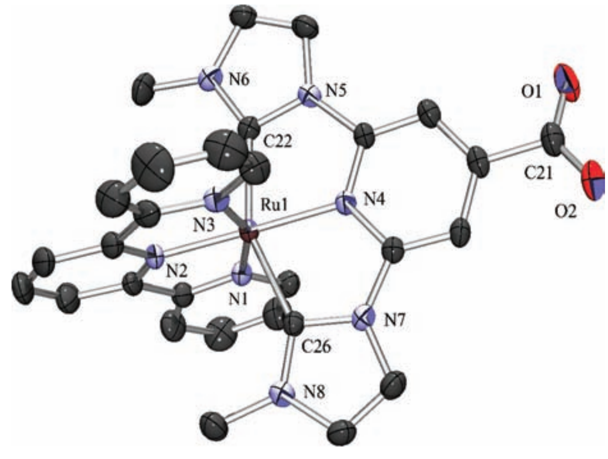

Figure 1. ORTEP drawing of **TCN**. The sovent molecules (four H_2O) and the counteranion (one PF_6^-) were omitted for clarity. Note that the carboxylic acid group is deprotonated. Selected bond lengths (Å) and angles (°) with estimated standard deviations: Ru(1)−N(1), 2.081(3); Ru(1)−N(2), 1.969(3); Ru(1)−N(3), 2.072(3); Ru(1)−C(22), 2.058(4); Ru(1)−N(4), 2.026(3); Ru(1)−C(26), 2.051(4); C(21)−O(1), 1.245(6); C(22)−O(1), 1.243(6); N(1)−Ru(1)−N(3), 157.12(13); C(22)−Ru(1)−C(22), 153.81(15); N(2)−Ru(1)−N(4), 177.89(13).

Electronic Absorption Spectroscopy. The electronic absorption spectra of **BCN**, **TCN**, and **CTN** in acetonitrile at room temperature are shown in Figure 2; the corresponding λ_{max} values as well as extinction coefficients are listed in Table 1. As we anticipated, the gradual red shift of λ_{max} manifested in the order **CTN** > **TCN** > **BCN**; the absorption maxima of **CTN**, **TCN**, and **BCN** appeared at 463, 448, and 430 nm, respectively, and the corresponding degrees of red shift from their archetypal complex $[Ru(bip)_2]^{2+}$ were 4580, 3857, and 2922 cm^{-1}. It should be noted that the spectral red shift of **BCN** is already near 3000 cm^{-1} due to the influence of an electron-withdrawing carboxylic acid group on the pyridyl ring. The influence of this carboxylic acid group on the electronic structure of frontier MOs will be discussed in more detail in the Computational Calculation Section.

The spectral envelope of **CTN**'s lowest energy absorption band is very broad, suggesting that this band is an overlap of multiple peaks. The spectrum of **TCN** also exhibited shoulders at 520 and 470 nm besides a λ_{max} at 448 nm. These results indicate that the origins of the λ_{max} of both **TCN** and **CTN** do not stem from the simple HOMO-to-LUMO transitions. On the other hand, the spectrum of **BCN** exhibits a clear Gaussian peak at 430 nm. The different pattern of optical transitions of the three complexes, despite their structural similarities to each other, has prompted our investigation of the origin of such behaviors. Further details of the results will be discussed later in this paper.

Despite the similar structural motif, the three complexes have quite different absorption intensities; the magnitude of the extinction coefficient of **BCN** was 28 100 $M^{-1}cm^{-1}$, while those of **TCN** and **CTN** were

---

(72) Smalley, S. J.; Waterland, M. R.; Telfer, S. G. *Inorg. Chem.* **2009**, *48*, 13–15.

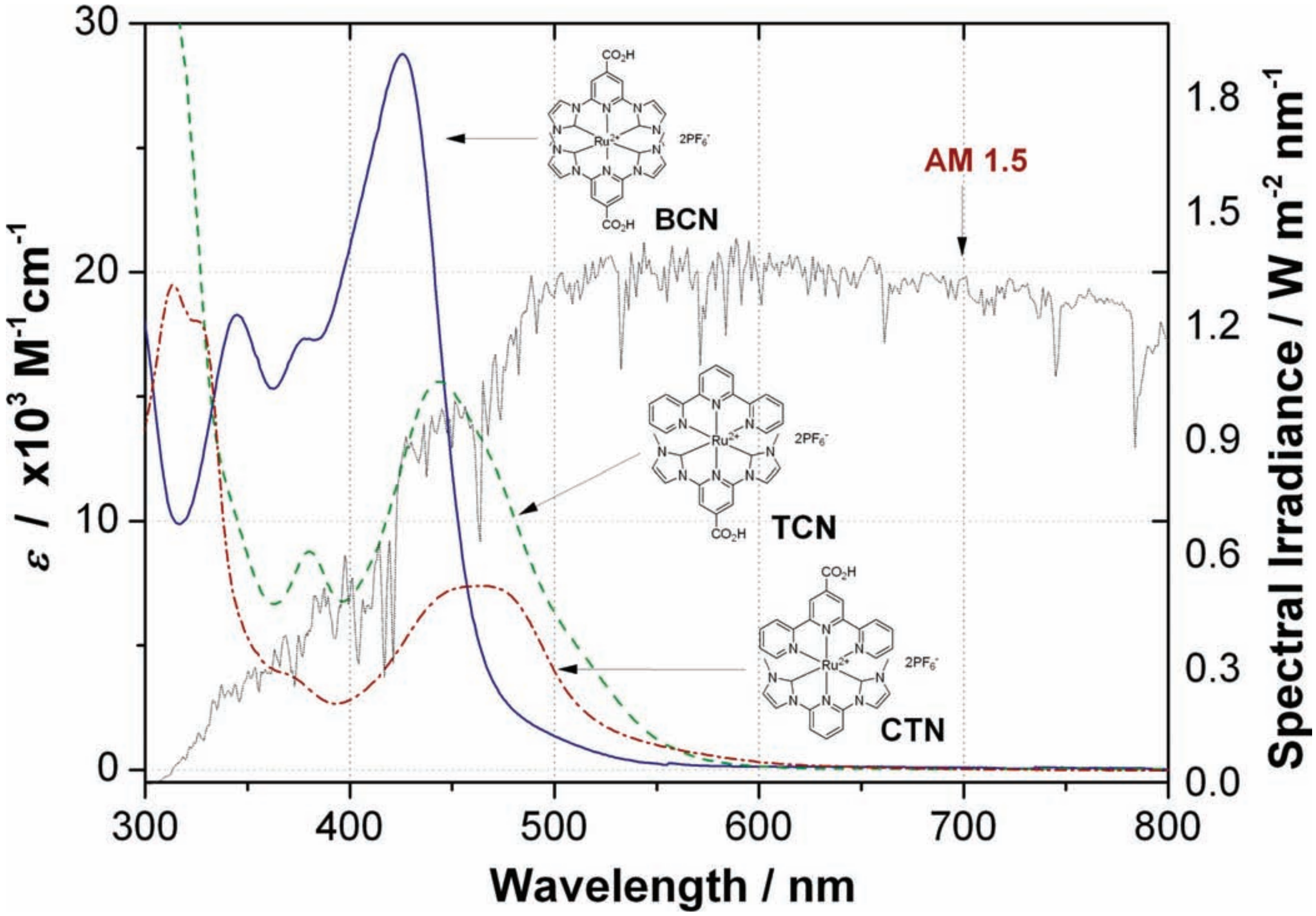

Figure 2. Electronic absorption spectra of **BCN** (solid blue), **TCN** (dashed green), and **CTN** (dash-dotted red) complexes. Solar spectral irradiance (AM 1.5) is shown in gray line. Experimental conditions: solvent = acetonitrile, temperature = 23 °C.

Table 1. Spectroscopic and Voltammetric Data

	$\lambda_{\max}$[a]		ε	$E(0,0)$	$E_{1/2}^{\text{ox}}$[b]
complex	nm	cm^{-1}	$\times 10^4\ \text{M}^{-1}\text{cm}^{-1}$	EV	V vs NHE
BCN	430	23 256	2.81	2.77[c]	1.78
TCN	448	22 321	1.54	2.64[c]	1.79
CTN	463	21 598	0.74	2.54[c]	1.79
$[\text{Ru(bip)}_2]^{2+}$[d]	382	26 178	1.52	3.37	1.38
$[\text{Ru(tpy)}_2]^{2+}$[d]	474	21 097	1.72		1.55[e]

[a] Experimental conditions: solvent = acetonitrile, and temperature = 23 °C. [b] Experimental conditions: [compound] = 5 mM; [TBAPF_6] = 0.1 M; solvent = acetonitrile; temperature = 23 °C; scan rate = 100 mV/s; reference electrode = Ag/Ag^+; and working electrode = glassy carbon. All potentials are referenced to a ferrocene/ferrocenium redox couple as an internal standard and converted to NHE by the relation ferrocene/ferrocenium vs NHE = +0.64 V. [c] Estimated values by $\lambda_{\max} - 1100\ \text{cm}^{-1}$. [d] From ref 22. [e] In ref 73, it was reported to be 1.52 V.

15 400 and 7400 $\text{M}^{-1}\text{cm}^{-1}$, respectively. A factor of almost two in the extinction coefficient of **BCN** relative to $[\text{Ru(bip)}_2]^{2+}$ (15,200 $\text{M}^{-1}\text{cm}^{-1}$) is noteworthy. However, the sharp decrease in the extinction coefficients of **CTN** is unexpected. Both **TCN** and **CTN** have one bip and one tpy ligand. The only difference between these two is the position of the carboxylic acid group, which eventually gives rise to a huge difference in absorption efficiency.

Electrochemistry. Electrochemical oxidation potentials of the three complexes in acetonitrile at 23 °C were recorded, and their values are listed in Table 1.[73] The one-electron reversible oxidations of **BCN**, **TCN**, and **CTN** occur at 1.78, 1.79, and 1.79 V, respectively. This result is somewhat striking; the first oxidation potential of **BCN** has been shifted positively by 0.4 V from that of $[\text{Ru(bip)}_2]^{2+}$. Considering the fact that the structural difference between **BCN** and $[\text{Ru(bip)}_2]^{2+}$ is only two carboxylic groups, the magnitude of the positive shift of the first oxidation potential is remarkable. As a result, the oxidation potential of **BCN** is even more positive than that of $[\text{Ru(tpy)}_2]^{2+}$ by at least 0.2 V, which indicates that the electron-donating effect of bip is no longer stronger than tpy when a carboxylic acid group is attached. The abrupt change of the electron-donating effect due to the incorporation of a carboxylic acid group is unusual. For example, the first oxidation potential of $[\text{Ru(tpy-CO}_2\text{H)}_2]^{2+}$ was reported to be 1.65 V, which is only 0.13 V higher than that of $[\text{Ru(tpy)}_2]^{2+}$.[74]

Another interesting thing is that the first oxidation potentials of the three complexes are virtually identical regardless of the ligand composition. Since the first oxidations of these complexes occur by the removal of an electron from the metal-centered HOMO, the similar oxidation potentials of the three complexes imply that the energy levels of the HOMOs are also similar to each other.

---

(73) For the cyclic voltammograms, see Supporting Information.

(74) Koivisto, B. D.; Robson, K. C. D.; Berlinguette, C. P. *Inorg. Chem.* **2009**, *48*, 9644–9652.

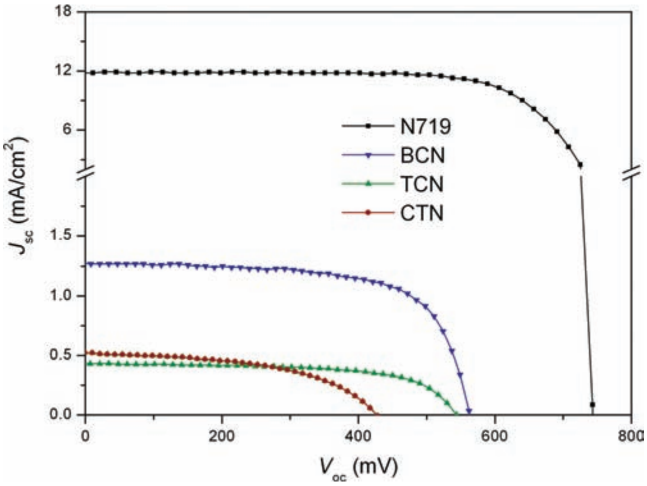

Figure 3. Photocurrent density versus voltage curve for DSSC systems of **BCN**, **TCN**, **CTN**, and N719 complexes under AM 1.5. The electrolyte was a mixture of 0.7 M BMII, 0.03 M I2, 0.1 M GSCN, and 0.5 M TBP in acetonitrile and valeronitrile (85:15). The active area of the dye-coated TiO_2 film was 0.420 cm^2.

The bip ligand was more electron donating than the tpy one when we compared the first oxidation potentials of $[Ru(bip)_2]^{2+}$ and $[Ru(tpy)_2]^{2+}$. By contrast, however, bip with a carboxylic group was rather less electron donating than tpy with the same group. This result indicates that NHC ligands are far more sensitive to the substituent, and thus the control window of electronic effect can be further expanded.

Photovoltaic Data. The overall efficiencies (η) of DSSC systems with **BCN**, **TCN**, and **CTN** as well as N719 as sensitizers were quantified using eq 1, with the values of short circuit photocurrent density (J_{SC}), the open circuit voltage (V_{OC}), and the fill factor (*ff*) taken from the $I-V$ relations (Figure 3):

$$\eta = J_{SC} \times V_{OC} \times \frac{ff}{I} \qquad (1)$$

where I is the intensity of the incident light (I = 1000 W/m^2). The fill factor is defined by eq 2:

$$ff = \frac{J_{max} \times V_{max}}{J_{SC} \times V_{OC}} \qquad (2)$$

where J_{max} and V_{max} are the photocurrent and the photovoltage for the maximum power, respectively. As shown in Table 2, the overall efficiencies of the DSSC systems of **BCN**, **TCN**, and **CTN** are 0.48, 0.14, and 0.10%, respectively. These values are significantly smaller than that of the N719 system, which showed 6.34% in our test. In detail, the J_{SC} values of **BCN**, **TCN**, and **CTN** systems were 1.27, 0.41, and 0.50 mA/cm^2, respectively, which are only 3.8−11.7% of that for the N719 system (10.89 mA/cm^2). The V_{OC} values of the same systems were 0.56, 0.54, and 0.41 V, which are 51−70% of the N719 system (0.80 V). In case of fill factors, the **BCN**, **TCN**, and **CTN** systems exhibited 67.3, 63.6, and 48.7%, respectively, while the N719 system did 72.8%. Thus the main reason for the low efficiencies of our systems is due to the low J_{SC} values with minor contribution from the V_{OC}s and fill factors. These results are well represented in Figure 3.

Table 2. Photovoltaic Data

complex	J_{SC} (mA/cm^2)[a]	V_{OC} (mV)[b]	fill factor	η (%)[c]
BCN	1.27 ± 0.01	561 ± 2	67.3 ± 0.3	0.48 ± 0.01
TCN	0.41 ± 0.02	540 ± 4	63.6 ± 0.8	0.14 ± 0.01
CTN	0.50 ± 0.03	407 ± 21	48.7 ± 1.5	0.10 ± 0.01
N719	10.9 ± 0.03	802 ± 8	72.8 ± 0.7	6.34 ± 0.03

[a] Short-circuit current. [b] Open-circuit voltage. [c] Overall cell efficiency.

It is important to note that the V_{OC} value of **CTN** is particularly smaller than the other two. **BCN** and **TCN** have a carboxylic acid anchoring group at the 4′ position of the pyridyl ring in the bip ligand. The V_{OC} values of these complexes were similar within 0.54−0.56 V range. By contrast, **CTN** has the carboxylic acid group at the 4′ position of the pyridyl ring in the tpy ligand and exhibited 0.41 V of V_{OC}. Since the V_{OC} value is related to the energy difference between the TiO_2 semiconductor conduction band edge and the redox potential of the I_2/I_3^- couple, the difference in V_{OC} value might be caused by the fluctuation of the TiO_2 conduction band edge. The smaller V_{OC} value of the **CTN** system relative to **BCN** or **TCN** ones is thus most likely due to the more stabilized conduction band edge of the TiO_2 surface. The detailed cause of the low V_{OC} value in the **CTN** system is not clear. Further investigation is necessary to resolve this problem.

To interrogate the background of low J_{SC} values of our systems relative to that of N719 one, we measured IPCE spectra. IPCE determined by J_{SC} divided by the incident photon flux Φ (mW/cm^2) at a monochromatic wavelength (λ) can be related to the light-harvesting efficiency (LHE), the quantum yield of electron injection (ϕ_{inj}), and the efficiency of collecting the injected electrons at the back contact (η_{coll}) as follows (eq 3):[75,76]

$$\mathrm{IPCE}(\%) = 1240\frac{J_{SC}}{\lambda\Phi} \times 100 = \mathrm{LHE}(\lambda)\varphi_{inj}\eta_{coll} \qquad (3)$$

Thus the proper evaluation of each parameter gives a clue for the elucidation of low J_{SC}. The LHE(λ) in turn can be calculated by the eq 4:[11,75,76]

$$\mathrm{LHE}(\lambda) = 1 - 10^{-1000\varepsilon\Gamma} = 1 - 10^{-\varepsilon c\rho d/10^7} \qquad (4)$$

where ε is the molar extinction coefficient, Γ is the number of moles of sensitizers per square centimeter of projected surface area of the film (mol/cm^2), c is the dye coverage (μmol/g), ρ is the density of nanocrystalline TiO_2 including dyes (assumed to be 3.84 g/cm^3), and d is the film thickness (μm). The overall features of IPCE spectra of the three systems are reminiscent of absorption spectra of their constituent complexes; the wavelengths of maximum IPCEs were 420, 450, and 470 nm for **BCN**, **TCN**, and **CTN** systems, respectively, which mirror the trend of the absorption maxima. However, the magnitudes of IPCEs of these systems differ significantly from each other and were far smaller than that of N719. In search of the factor that plays a most significant role in

---

(75) Nazeeruddin, M. K.; Kay, A.; Rodicio, I.; Humphrybaker, R.; Muller, E.; Liska, P.; Vlachopoulos, N.; Gratzel, M. *J. Am. Chem. Soc.* **1993**, *115*, 6382–6390.

(76) Gratzel, M. Nanocrystallline Injection Solar Cells. In *Thin Film Solar Cells: Fabrication, Characterization and Applications*; Poortmans, J., Arkhipov, V., Ed.; John Wiley & Sons, Ltd: West Sussex, England, 2006; pp 363−385.

Table 3. IPCE, Dye Concentration, LHE, and ϕ_{inj}

	IPCE[a]					
complex	$\lambda_{\max}$(nm)	%	dye coverage, μmol/g	Γ^b, $\times 10^7$ mol/cm^2	LHE[c]	ϕ_{inj}[d]
BCN	420	20.7	109.6	3.79	1.000	20.7
TCN	450	2.9	42.2	1.46	0.994	2.9
CTN	470	4.7	66.6	2.30	0.980	4.8
N719	520	62.0	65.2	2.25	0.999	62.0

[a] Incident photon-to-current efficiency. [b] The number of moles of sensitizers per square centimeter of projected surface area of the film. [c] Light-harvesting efficiency at maximum IPCE. [d] Charge injection efficiency.

determining the magnitude of IPCE, we examined three parameters, LHE, ϕ_{inj}, and η_{coll}. First, we calculated LHE values according to eq 4 (Table 3). We determined the dye coverage by means of inductively coupled plasma mass spectrometry (ICP-MS). The observed dye coverages were 109.6, 42.2, 66.6, and 65.2 μmol per 1 g of TiO_2 for the **BCN**, **TCN**, **CTN**, and N719 systems, respectively. The thicknesses of the films were determined by SEM. The representative SEM image is shown in the Supporting Information (Figure S2), which demonstrates the film thickness of ~9 μm. The resulting LHE values of four systems at maximum absorption wavelength were thus calculated and listed in Table 3. Interestingly, LHE values at the absorption maxima of four systems were found to be similar each other, which were all near 1 within 2% regardless of a factor of 4 different molar extinction coefficients of constituent sensitizers. It is because the thickness of the film reaches the level necessary to harvest incoming light almost completely. For example, the LHE of **CTN** system, which has the smallest molar extinction coefficient among the four systems, reaches 90% of LHE when the thickness of the film is only 5.3 μm and 97% at 8 μm at the given dye coverage. Therefore, it is apparent that LHE is not a major factor that discriminates the magnitude of IPCE, at least in our experiment. This feature is well represented in the absorption spectra of the DSSC system in which sensitizers are coated on the TiO_2 film (Supporting Information, Figure S3). See Figure 4 for the spectra of IPCEs.

It is well established that the collection of charge carrier is quantitative if the electron diffusion length exceeds the film thickness (d).[76] Since the diffusion length of TiO_2 is known to be several hundred μms and the film thicknesses of the systems used in our experiment are only ~9 μm, η_{coll} can be safely regarded as 1 for all systems. With the experimentally determined IPCEs along with the estimated LHE and η_{coll} values in hand, ϕ_{inj}s were calculated and listed in Table 3. As shown, IPCEs are strongly correlated with ϕ_{inj}s. Thus it is reasonable to conclude that the low IPCEs of our systems in general were caused by low ϕ_{inj}s. As eq 5 indicates, charge injection from the electronically excited sensitizer into the conduction band of the TiO_2 is in competition with other deactivation pathways that include radiative or nonradiative internal conversions, singlet-to-triplet intersystem crossings, and charge recombination reactions, etc.[76]

$$\varphi_{\mathrm{inj}} = \frac{k_{\mathrm{inj}}}{k_{\mathrm{inj}} + \sum_{\mathrm{deact}} k_{\mathrm{deact}}} \tag{5}$$

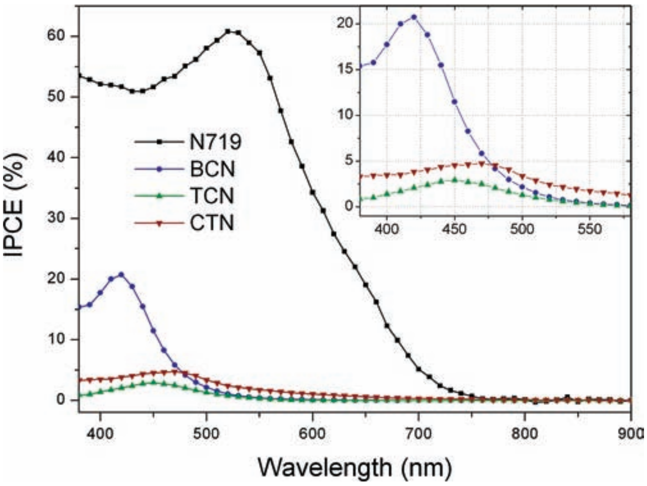

Figure 4. Spectra of monochromatic incident photon-to-current conversion efficiencies (IPCEs) for DSSC systems of **BCN**, **TCN**, **CTN**, and N719 complexes.

The detailed deactivation pathways are currently unavailable. Further studies on the excited-state dynamics of sensitizers on the TiO_2 film are necessary for the elucidation of those.

Computational Study. Ground-State Electronic Structure. The geometry optimization and electronic structure calculations of **BCN**, **TCN**, and **CTN** were performed via DFT. The energies of the frontier occupied and unoccupied MOs of the three new complexes are compared in Figure 5 along with those of $[Ru(bip)_2]^{2+}$ and $[Ru(tpy)_2]^{2+}$ benchmarks. In order to assign the character of the MOs, we first calculated the atomic orbital coefficients using Mulliken population analysis. The percent contribution of each atom was calculated according to eq 6, where n is the atomic orbital coefficient in a specific MO.[77]

$$\%\mathrm{contribution} = \frac{n^2}{\sum n^2} \times 100 \tag{6}$$

The calculated percent contributions of each atom in the five highest occupied and the three LUMOs are summed into three classes (Ru, **L-1**, and **L-2**, where **L-1** and **L-2** denote one of two tridentate ligands in the three new complexes) to judge which part of the complex possesses the dominant electron population (Table 4). The three-dimensional representations of the isosurfaces of each MO clearly confirm the character of the MO (Figure 6).

For all three complexes, the three HOMOs (153−155 for **BCN** and 140−142 for both **TCN** and **CTN**) are mainly ruthenium *d*-orbital in character, as in the case of $[Ru(tpy)_2]^{2+}$. It is important to note, however, that contributions from ruthenium metal in these three HOMOs remain only in the 50−60% range in **BCN** and 60−70% in **TCN** or **CTN**. The contributions from ligands are, therefore, substantial and thus cannot be ignored. On the other hand, the three LUMOs are basically π^* orbitals of bip or tpy ligands with or without carboxylic acid groups. Therefore, electronic transitions that involve these frontier

---

(77) Stoyanov, S. R.; Villegas, J. M.; Rillema, D. P. *Inorg. Chem.* **2003**, *42*, 7852–7860.

orbitals possess the intrinsic $\pi-\pi^*$ or ligand-to-ligand charge transfer (LLCT) character, even though their main characters are MLCT.

Due to the structural symmetry, frontier MOs of **BCN** contain a certain amount of degeneracy; the two LUMOs (MO 156 and 157) and HOMO-1/HOMO-2 couple (MO 153 and 154) are degenerate. In the case of the two LUMOs, the electronic population is mainly localized in the central pyridyl ring, including the carboxylic acid group. On the other hand, the HOMO-1/HOMO-2 couple contains ~40% of the electronic population on two ligands equally divided and spread over each half. The remaining ~60% of the electronic population is localized in the ruthenium metal. In the HOMO, only 50% of the electronic population is localized in the ruthenium metal. Each ligand contains ~25% of the electronic population with slightly being more dominant in two imidazol rings.

The ground-state electronic structures of **TCN** and **CTN** contain little degeneracy, as anticipated from their structural asymmetry. Only LUMO and LUMO+1 of the **TCN** complex are quasidegenerate. The characters and energies of the three HOMOs of these complexes resemble each other. At least in terms of the ligand part, the electronic population is dominant in the bip ligand in HOMO and HOMO-2 and in the tpy ligand in HOMO-1. The differences appear in the energies of the unoccupied MOs. The essential character of the LUMO of each complex is virtually similar. The electronic population is mainly localized in the tpy ligand in the LUMOs of both complexes. However, the LUMO of **CTN** is lower in

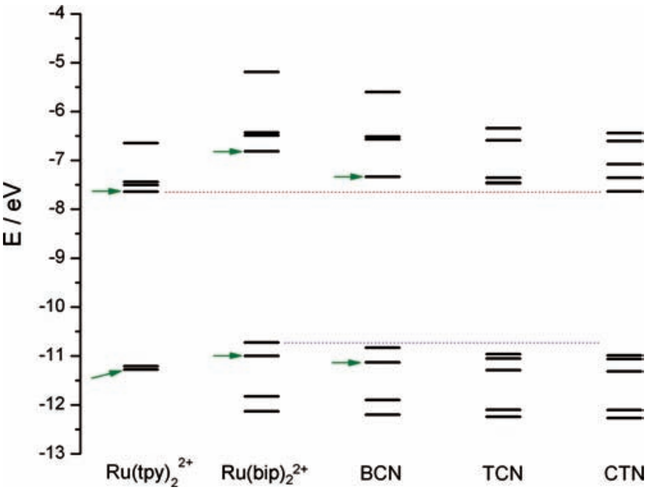

Figure 5. Frontier molecular orbital (five highest occupied and five lowest unoccupied) energy diagram of $[Ru(tpy)_2]^{2+}$, $[Ru(bip)_2]^{2+}$, **BCN**, **TCN**, and **CTN** calculated at the B3LYP/LANL2DZ level. Green arrows denote degeneracy. HOMO energy level of $[Ru(bip)_2]^{2+}$ and LUMO energy level of $[Ru(tpy)_2]^{2+}$ are guided by blue and red dotted lines, respectively.

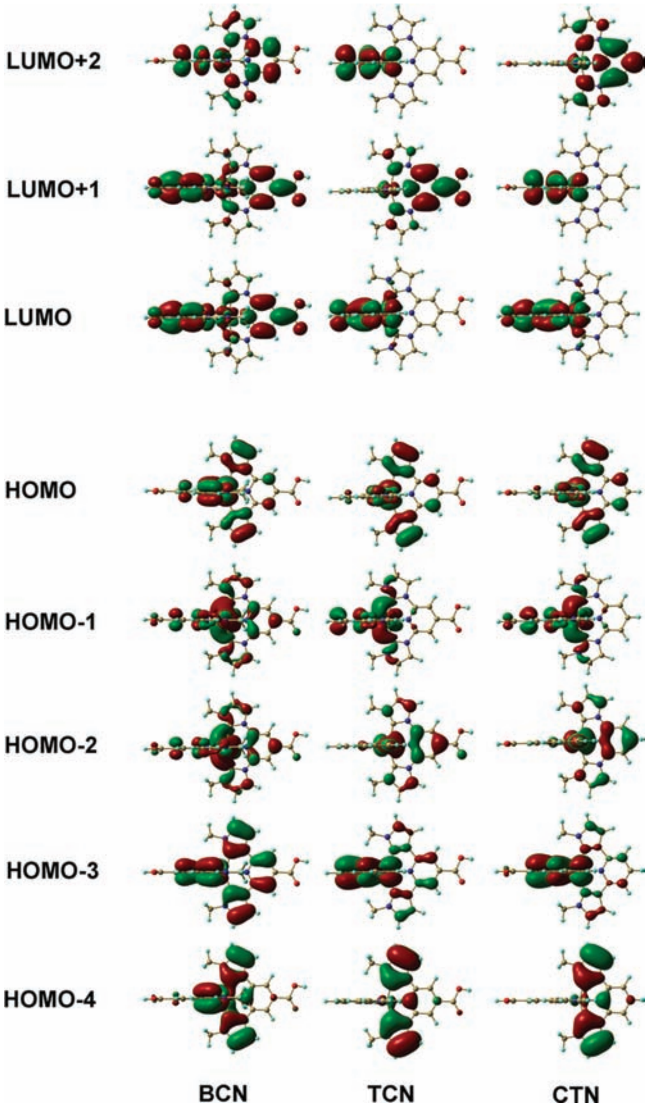

Figure 6. Three-dimensional representation of frontier molecular orbital isosurfaces calculated at the B3LYP/LANL2DZ level.

Table 4. Energies and % Compositions of Frontier MOs of **BCN**, **TCN**, and **CTN**

BCN					TCN					CTN				
MO		percent composition			MO		percent composition			MO		percent composition		
no.	E (eV)	Ru	L-1[a]	L-2[a]	no.	E (eV)	Ru	L-1[a]	L-2[b]	no.	E (eV)	Ru	L-1[c]	L-2[d]
3[e] (158)	−6.57	0.00	50.00	50.00	3[e] (145)	−7.36	1.33	0.79	97.88	3[e] (145)	−7.08	8.24	86.02	5.74
2[e] (157)	−7.34	8.23	44.83	46.94	2[e] (144)	−7.46	8.09	87.29	4.62	2[e] (144)	−7.36	1.29	0.87	97.83
1[e] (156)	−7.34	8.23	46.94	44.83	1[e] (143)	−7.47	9.32	6.67	84.01	1[e] (143)	−7.64	10.60	18.35	71.05
0[e] (155)	−10.83	50.08	25.96	24.96	0[e] (142)	−10.96	59.28	31.97	8.76	0[e] (142)	−10.99	59.34	31.84	8.81
−1[e] (154)	−11.13	60.84	19.55	19.60	−1[e] (141)	−11.05	63.82	19.03	17.15	−1[e] (141)	−11.06	62.35	23.11	14.54
−2[e] (153)	−11.13	60.85	19.60	19.55	−2[e] (140)	−11.29	72.34	16.35	11.31	−2[e] (140)	−11.31	73.31	15.13	11.56
−3[e] (152)	−11.90	0.03	49.98	49.98	−3[e] (139)	−12.10	0.19	9.75	90.06	−3[e] (139)	−12.10	0.12	9.18	90.70
−4[e] (151)	−12.20	7.90	46.04	46.06	−4[e] (138)	−12.24	4.30	93.70	2.00	−4[e] (138)	−12.27	4.37	93.55	2.08

[a] Bip-CO_2H ligand. [b] Tpy ligand. [c] Bip ligand. [d] Tpy-CO_2H ligand. [e] HOMO and LUMO are 0 and 1, respectively, and −1, −2, ..., −4 correspond to HOMO-1, HOMO-2, ..., HOMO-4, respectively, while 2 and 3 represent LUMO+1 and LUMO+2, respectively.

Table 5. Composition of the Excited-State Wave Functions of **BCN**, **TCN**, and **CTN** in Terms of the Linear Combination Coefficients in the Configuration Expansion[a]

	energy				
state[b]	eV	cm^{-1}	f[c]	wave function	major character
				BCN	
S5[d]	3.07	24 756	0.4113	$0.43\ \Psi_{-2\rightarrow1} + 0.19\ \Psi_{-2\rightarrow2} - 0.19\ \Psi_{-1\rightarrow1} + 0.43\ \Psi_{-1\rightarrow2} + 0.15\ \Psi_{0\rightarrow3}$	MLCT
S7	3.59	28 978	0.2623	$0.68\ \Psi_{0\rightarrow3}\ +$	MLCT
S13	3.88	31 291	0.0232	$-0.32\ \Psi_{-3\rightarrow1} + 0.49\ \Psi_{-3\rightarrow2} + 0.22\ \Psi_{-1\rightarrow3} + 0.25\ \Psi_{-1\rightarrow4}$	$\pi-\pi^*$
S14	3.88	31 292	0.0232	$0.49\ \Psi_{-3\rightarrow1} + 0.32\ \Psi_{-3\rightarrow2} - 0.22\ \Psi_{-2\rightarrow3} + 0.25\ \Psi_{-2\rightarrow3}$	$\pi-\pi^*$
S15	4.06	32 709	0.0197	$0.33\ \Psi_{-5\rightarrow1} - 0.36\ \Psi_{-5\rightarrow2} + 0.37\ \Psi_{-4\rightarrow1} + 0.33\ \Psi_{-4\rightarrow2}$	$\pi-\pi^*$
				TCN	
S1	2.54	20 502	0.0011	$0.69\ \Psi_{0\rightarrow1}$	MLCT
S3	2.65	21 397	0.0073	$0.69\ \Psi_{0\rightarrow2}$	MLCT
S4[d]	2.86	23 094	0.0506	$0.12\ \Psi_{-2\rightarrow1} + 0.54\ \Psi_{-1\rightarrow2} + 0.42\ \Psi_{0\rightarrow3}$	MLCT
S6[d]	2.96	23 850	0.0539	$0.69\ \Psi_{-1\rightarrow3}$	MLCT
S7[d]	3.02	24 331	0.2338	$-0.39\ \Psi_{-2\rightarrow1} - 0.27\ \Psi_{-1\rightarrow2} + 0.50\ \Psi_{0\rightarrow3}$	MLCT
S8	3.19	25 706	0.0063	$0.48\ \Psi_{-2\rightarrow1} - 0.26\ \Psi_{-1\rightarrow2} + 0.25\ \Psi_{0\rightarrow3} + 0.28\ \Psi_{0\rightarrow4} - 0.11\ \Psi_{0\rightarrow6}$	MLCT
S13	3.75	30 277	0.1651	$-0.18\ \Psi_{-2\rightarrow1} + 0.60\ \Psi_{0\rightarrow4} + 0.22\ \Psi_{0\rightarrow6}$	MLCT
S14	3.78	30 462	0.002	$0.24\ \Psi_{-5\rightarrow1} + 0.13\ \Psi_{-3\rightarrow1} + 0.61\ \Psi_{-2\rightarrow4} + 0.19\ \Psi_{-1\rightarrow8}$	MLCT
S15	3.89	31 403	0.0173	$-0.44\ \Psi_{-3\rightarrow2} + 0.53\ \Psi_{0\rightarrow5}$	LLCT
S16	3.94	31 811	0.0139	$-0.19\ \Psi_{-5\rightarrow1} - 0.27\ \Psi_{-3\rightarrow1} - 0.15\ \Psi_{-2\rightarrow6} + 0.55\ \Psi_{-1\rightarrow8} - 0.11\ \Psi_{-1\rightarrow10}$	MLCT
S17	3.97	32 040	0.0039	$0.12\ \Psi_{-3\rightarrow3} + 0.68\ \Psi_{-1\rightarrow5}$	MLCT
S20	4.02	32 394	0.0064	$0.68\ \Psi_{-4\rightarrow1} - 0.16\ \Psi_{0\rightarrow6}$	LLCT
S21	4.08	32 900	0.4075	$0.11\ \Psi_{-5\rightarrow2} + 0.49\ \Psi_{-3\rightarrow2} + 0.14\ \Psi_{-1\rightarrow6} + 0.42\ \Psi_{0\rightarrow5}$	LLCT + MLCT
				CTN	
S1	2.38	19 192	0.0032	$0.69\ \Psi_{0\rightarrow1}$	MLCT
S3[d]	2.73	22 027	0.0797	$0.54\ \Psi_{-1\rightarrow1} + 0.41\ \Psi_{0\rightarrow2}$	MLCT
S4[d]	2.90	23 381	0.0472	$0.69\ \Psi_{-1\rightarrow2}$	MLCT
S5[d]	2.98	24 038	0.1741	$-0.11\ \Psi_{-2\rightarrow3} - 0.34\ \Psi_{-1\rightarrow1} + 0.56\ \Psi_{0\rightarrow2}$	MLCT
S6	3.04	24 489	0.0077	$-0.13\ \Psi_{-2\rightarrow2} + 0.68\ \Psi_{0\rightarrow3}$	MLCT
S9	3.53	28 458	0.0211	$0.57\ \Psi_{-2\rightarrow3} - 0.38\ \Psi_{0\rightarrow5}$	MLCT
S11	3.69	29 769	0.0067	$-0.33\ \Psi_{-3\rightarrow1} + 0.54\ \Psi_{-2\rightarrow8} - 0.14\ \Psi_{-2\rightarrow10} + 0.12\ \Psi_{-1\rightarrow5} - 0.18\ \Psi_{0\rightarrow4}$	MLCT
S12	3.74	30 143	0.0111	$0.36\ \Psi_{-3\rightarrow1} + 0.32\ \Psi_{-2\rightarrow8} + 0.12\ \Psi_{-1\rightarrow5} + 0.46\ \Psi_{0\rightarrow4}$	MLCT
S14	3.85	31 035	0.0776	$-0.12\ \Psi_{-3\rightarrow2} + 0.66\ \Psi_{-1\rightarrow4} - 0.13\ \Psi_{0\rightarrow5}$	MLCT
S15	3.87	31 188	0.2161	$0.20\ \Psi_{-5\rightarrow1} + 0.45\ \Psi_{-3\rightarrow1} + 0.12\ \Psi_{-2\rightarrow8} - 0.44\ \Psi_{0\rightarrow4}$	MLCT+$\pi-\pi^*$
S16	3.87	31 241	0.1403	$0.25\ \Psi_{-2\rightarrow3} + 0.15\ \Psi_{-1\rightarrow4} + 0.50\ \Psi_{0\rightarrow5} + 0.33\ \Psi_{0\rightarrow6}$	MLCT
S17	3.90	31 475	0.0098	$-0.12\ \Psi_{-5\rightarrow3} + 0.59\ \Psi_{-2\rightarrow5} - 0.16\ \Psi_{-2\rightarrow6} - 0.30\ \Psi_{-1\rightarrow8}$	MLCT
S19	3.97	32 020	0.1441	$0.64\ \Psi_{-5\rightarrow1} + 0.19\ \Psi_{0\rightarrow4}$	MLCT
S21	4.02	32 403	0.0455	$0.68\ \Psi_{-1\rightarrow6}$	MLCT
S23	4.11	33 199	0.0059	$0.15\ \Psi_{-5\rightarrow2} - 0.18\ \Psi_{-2\rightarrow3} + 0.12\ \Psi_{-1\rightarrow7} - 0.22\ \Psi_{0\rightarrow5} + 0.56\ \Psi_{0\rightarrow5}$	MLCT

[a] Only oscillator strengths larger than 0.001 and up to 33 333 cm^{-1} are reported. Subscripts correspond to the following orbitals: The highest occupied orbitals have an index 0, i.e., 0 = HOMO, while all other occupied orbitals have index −1, −2, ..., −*n*, which corresponds to HOMO-1, HOMO-2, ..., HOMO-*n*, respectively. LUMO = 1, LUMO+1 = 2, LUMO+2 = 3, and so on. [b] State numbers obtained from the calculation. [c] Oscillator strength. [d] State mostly responsible for the low energy absorption band.

energy (0.17 eV) relative to that of **TCN**, probably due to the existence of the electron-withdrawing carboxylic acid group. As shown in Figure 6, the electronic population in the LUMO of **CTN** is apparently delocalized over the whole tpy ligand, including the carboxylic acid group, while that of **TCN** is only confined within the tpy ring system. In a similar manner, the LUMO+1 of **TCN**, in which the majority of the electronic population is spread over the whole bip ligand including the carboxylic acid, is significantly lower in energy (0.38 eV) relative to the LUMO+2 of **CTN**, which does not have a carboxylic acid group in the bip ligand. Interestingly, the LUMO+1 of **CTN** is isoenergetic with the LUMO+2 of **TCN**; these frontier MOs have the majority of their electronic population in the tpy part with only the former having a carboxylic acid group in that ligand. Nevertheless, the electronic population in the LUMO+1 of **CTN** is not delocalized over the carboxylic acid group but is only confined within the tpy ring system. As a result, the shape of the isosurface as well as the energy of this MO is almost similar to that of the LUMO+2 of **TCN**.

Our initial idea to accomplish spectral red-shift was by reducing the HOMO−LUMO gap through employing the hybrid ligand system in which the energy levels of the frontier MOs are varied from those of $[\mathrm{Ru(bip)_2}]^{2+}$. As clearly shown in Figure 5 (dotted blue line for the HOMO energy level of $[\mathrm{Ru(bip)_2}]^{2+}$ and dotted wine-red line for the LUMO energy level of $[\mathrm{Ru(tpy)_2}]^{2+}$), the desired electronic structures appear to be realized in **CTN**. The energy level of tpy-localized LUMO is virtually the same as that of $[\mathrm{Ru(tpy)_2}]^{2+}$, while that of ruthenium-centered HOMO is only ca. 0.11 eV more stabilized than that of $[\mathrm{Ru(bip)_2}]^{2+}$. As a result, the overall HOMO−LUMO gap of **CTN** becomes 3.35 eV, which is 0.19 and 0.55 eV smaller than those of $[\mathrm{Ru(tpy)_2}]^{2+}$ and $[\mathrm{Ru(bip)_2}]^{2+}$, respectively.

It is worth noting that the degenerate LUMO and LUMO+1 of **BCN** were substantially lower in energy (ca. 0.52 eV) than those of $[\mathrm{Ru(bip)_2}]^{2+}$. The electron population of these MOs of $[\mathrm{Ru(bip)_2}]^{2+}$ is mainly localized in the pyridyl ring. The incorporation of carboxylic acid at the four-position of the pyridyl ring drives the electronic delocalization over the pyridine carboxylic acid moiety very easily, and thus the energy of this MO can be stabilized. By contrast, the influence of the carboxylic acid group on the energy levels of HOMO of **BCN** is minimal (Figure 5). As shown in Figure 6, the electronic population in the HOMO of **BCN** is mainly localized in the ruthenium metal and the two imidazole rings, indicating that the carboxylic acid group on the pyridyl ring did not affect the electronic distribution as well as the energy level of this orbital significantly. Given this result, the voltammetrically determined first oxidation potential of **BCN**, which is 0.4 V more positive than that of $[Ru(bip)_2]^{2+}$, appears to be remarkable. Further investigation is necessary for the elucidation of this discrepancy between the experimentally observed and theoretically predicted HOMO energy levels of **BCN** relative to that of $[Ru(bip)_2]^{2+}$.

Electronic Absorption Spectra. The singlet electronic excited states of these complexes were calculated via a TD-DFT approach based on the optimized ground structure.[78] To take into account the solvent effect, we employed the conductor-like polarizable continuum model (CPCM) model.[79,80] For each complex, we considered 30 excited states. Transitions that have oscillator strengths larger than 0.001 are listed in Table 5. The calculated energy of each excited state is the vertical excitation. The absolute magnitudes of these energies do not overlap closely with those determined experimentally; the magnitudes of the energy differences between the experimental and calculated lowest absorption maxima were found to be 2200−2500 cm^{-1}. Nevertheless, the simulated spectra mirror well the experimental one (Figure 7).

For the spectral simulation, each excited state listed in Table 5 was represented as a Gaussian curve. These curves were summed into one line, and the result is illustrated in Figure 7. In the spectral simulation, it is important to choose a proper full-width at half-maximum (fwhm) for the successful reproduction of experimental results. Monat et al.[81] adopt ∼0.4 eV (∼3200 cm^{-1}) as a fwhm for the spectral simulation of the bis(4,4′-dicarboxylato-2,2′-bipyridine)bis(isothiocyanato)ruthenium(II) complex based on the preceding work regarding $Na_2[Fe(bpy)(CN)_4]$ by Yang et al.[82] Applying the same magnitude of fwhm evenly to each Gaussian curve of our three systems, however, made the simulated spectra too broad, which made us unable to distinguish each constituent peak clearly. Therefore, we applied 1000 cm^{-1} of fwhm value to all Gaussian curves for the spectral simulation with more emphasis on the identification of the constituent peaks.

The main purpose of this calculation was the characterization of the excited states that were responsible for constructing the spectral envelope in the lowest energy region. More specifically, we attempted to examine how the changes in energy of the frontier MOs of the three new complexes from their archetypal $[Ru(bip)_2]^{2+}$ affect the spectral features. As revealed by a number of preceding reports, the excited states calculated in this work demonstrated that most of the excited-state electronic structures can be best described in terms of a linear combination of multiple one-electron transitions, implying that a simple HOMO−LUMO energy gap cannot be linearly correlated to the electronic transition energy of the lowest energy absorption maximum.[41,74,81,83−91] For example, the S1 excited state of the **TCN** complex turned out to be a one-electron excitation from HOMO to LUMO. However, the oscillator strength of this transition is only 0.0011 and thus makes only a negligible contribution to the spectrum. The experimental peak maximum observed at 448 nm can be correlated to the S7 state wherein three transitions are mixed and give rise to 0.2338 of oscillator strength. A similar pattern was observed in **CTN**. In **BCN**, the S5 state has the largest oscillator strength (0.4113) among the investigated states and thus can be correlated to the experimental absorption maximum at 430 nm. This state is also comprised of five transitions, and the electronic excitation from HOMO to LUMO is not included in this state.

The characters of the excited states shown in the last column of Table 5 are classified as MLCT, $\pi-\pi^*$, LLCT, or mixed states of these, according to the nature of the occupied and unoccupied MOs involved in the electronic excitation. One important result in the delineation of the character of the excited states is the identification of the direction of the transition dipole moment. Since these complexes are designed for DSSC application, we hypothesized that the direction of the transition dipole moment is closely related to the electron injection efficiency from the sensitizer to the semiconductor. The sensitizer that has a large transition dipole moment directed toward the carboxylic acid anchoring group might be more efficient in electron injection than that with a transition dipole moment directed toward the opposite direction, if other conditions are identical. The magnitudes and directions of the transition dipole moments of the most representative states that correspond to the lowest energy absorption maxima are illustrated in Figure 8. For the S5 state of both **BCN** and **CTN** (Figure 8a and c, respectively), the transition dipole

---

(78) Although it is commonly found that a fast intersystem crossing occurs from a singlet excited state to a triplet one in this type of Ru complex and thus most of the emissions root from the triplet excited state manifold, we did not calculate triplet excited states since singlet → triplet transitions are spin forbidden, and thus those transitions would contribute, if any, only little to the electronic absorption spectrum.

(79) Barone, V.; Cossi, M. *J. Phys. Chem. A* **1998**, *102*, 1995–2001.

(80) Cossi, M.; Rega, N.; Scalmani, G.; Barone, V. *J. Comput. Chem.* **2003**, *24*, 669–681.

(81) Monat, J. E.; Rodriguez, J. H.; McCusker, J. K. *J. Phys. Chem. A* **2002**, *106*, 7399–7406.

(82) Yang, M.; Thompson, D. W.; Meyer, G. J. *Inorg. Chem.* **2000**, *39*, 3738–3739.

(83) Turki, M.; Daniel, C.; Zalis, S.; Vlcek, A.; van Slageren, J.; Stufkens, D. J. *J. Am. Chem. Soc.* **2001**, *123*, 11431–11440.

(84) Zalis, S.; Ben Amor, N.; Daniel, C. *Inorg. Chem.* **2004**, *43*, 7978–7985.

(85) Persson, P.; Lundqvist, M. J. *J. Phys. Chem. B* **2005**, *109*, 11918–11924.

(86) Nazeeruddin, M. K.; Wang, Q.; Cevey, L.; Aranyos, V.; Liska, P.; Figgemeier, E.; Klein, C.; Hirata, N.; Koops, S.; Haque, S. A.; Durrant, J. R.; Hagfeldt, A.; Lever, A. B. P.; Gratzel, M. *Inorg. Chem.* **2006**, *45*, 787–797.

(87) Ghosh, S.; Chaitanya, G. K.; Bhanuprakash, K.; Nazeeruddin, M. K.; Gratzel, M.; Reddy, P. Y. *Inorg. Chem.* **2006**, *45*, 7600–7611.

(88) Barolo, C.; Nazeeruddin, M. K.; Fantacci, S.; Di Censo, D.; Comte, P.; Liska, P.; Viscardi, G.; Quagliotto, P.; De Angelis, F.; Ito, S.; Gratzel, M. *Inorg. Chem.* **2006**, *45*, 4642–4653.

(89) Vlcek, A.; Zalis, S. *Coord. Chem. Rev.* **2007**, *251*, 258–287.

(90) De Angelis, F.; Fantacci, S.; Selloni, A.; Nazeeruddin, M. K.; Gratzel, M. *J. Am. Chem. Soc.* **2007**, *129*, 14156–14157.

(91) McCall, K. L.; Jennings, J. R.; Wang, H. X.; Morandeira, A.; Peter, L. M.; Durrant, J. R.; Yellowlees, L. J.; Woollins, J. D.; Robertson, N. *J. Photochem. Photobiol., A* **2009**, *202*, 196–204.

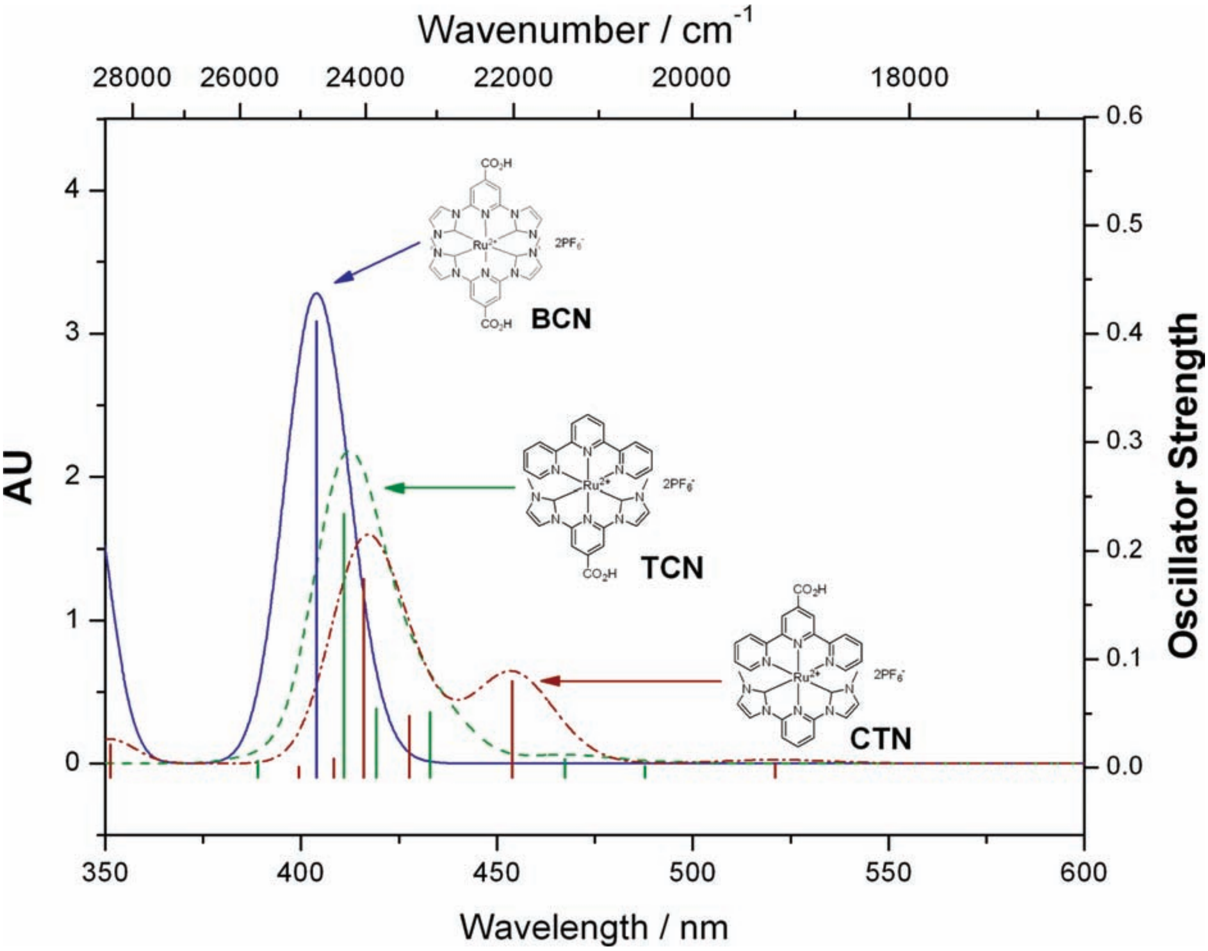

Figure 7. Simulated electronic absorption spectra of **BCN**, **TCN**, and **CTN** via TD-DFT method. Same basis sets and effective core potentials were used as those for the ground-state calculations. To take into account the solvation effect, CPCM implemented in the Gaussian 03 program package was used. Vertical lines represent oscillator strength of **BCN** (blue), **TCN** (green), and **CTN** (red). Peak shape of individual transition was assumed to be a Gaussian curve with full width at half-maximum (fwhm) of 1000 cm^{-1}.

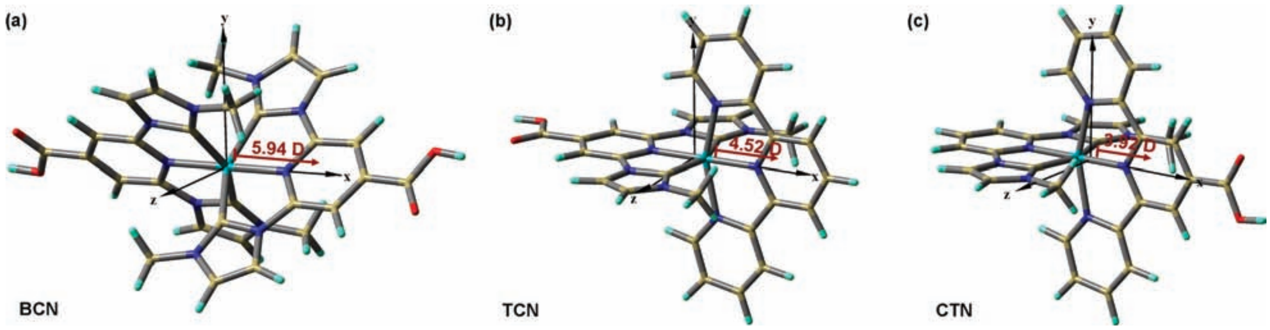

Figure 8. Transition dipole moments of (a) S5 state of **BCN**, (b) S7 state **TCN**, and (c) S5 state of **CTN**.

moments are directed toward the positive x direction, to which the carboxylic acid anchoring groups are attached. By contrast, S7 state of **TCN** has a transition dipole moment directed opposite to that of the carboxylic acid anchoring group. These features are in good agreement with the ϕ_{inj} as well as IPCE values at maximum wavelength (Table 3 and Figure 4). Not surprisingly, **BCN** has the largest ϕ_{inj} and IPCE value (20.7% for both), since the S5 state of this complex has the largest transition dipole moment, and its direction is toward the semiconductor interface. An interesting comparison can be made between **TCN** and **CTN**. The transition dipole moment of the S7 state of **TCN** (4.52 D) is larger in magnitude than that of the S5 state of **CTN** (3.92 D), as revealed by the experimentally determined molar extinction coefficients. Nevertheless, the measured IPCE of **TCN** (2.9%) is rather smaller than that of **CTN** (4.8%) due to the smaller magnitude of ϕ_{inj}, which proves our hypothesis that the direction of the transition dipole moment is closely related to the electron injection efficiency.

Conclusion

In order to manipulate the electronic transition energy of the previously reported [Ru(bip)$_2$]$^{2+}$ complex, we have incorporated different types of tridentate ligands with an anticipation that these hybrid ligand systems would give rise to the reduction of the HOMO−LUMO gap. Three new complexes, bis[2,6-bis(3-methylimidazol-3-ium-1-yl)pyridine-4-carboxylic acid]ruthenium(II) (**BCN**), [2,6-bis(3-methylimidazolium-1-yl)pyridine-4-carboxylic acid](2,2′;6′2″-terpyridine)-ruthenium(II) (**TCN**), and [2,6-bis(3-methylimidazol-3-ium-1-yl)pyridine](2,2′;6′2″-terpyridine-4′-carboxylic acid)ruthenium-(II) (**CTN**), have been synthesized according to this design strategy and fully characterized. Depending on the ligand compositions, the lowest energy electronic absorption bands of the three complexes were red-shifted by 3000−4500 cm^{-1} relative to that of $[Ru(bip)_2]^{2+}$. **CTN** with the bip- and tpy-CO_2H ligands exhibited the largest degree of red-shift. Theoretical density functional theory (DFT) calculation predicted that both the occupied and unoccupied molecular orbitals (MOs) of these complexes would be stabilized relative to those of $[Ru(bip)_2]^{2+}$. However, the degree of stabilization in the unoccupied MOs is much larger than that of destabilization in the occupied MOs. Moreover, the stabilization of the LUMO energy of **CTN** was found to be most significant. As a result, the lowest unoccupied molecular orbital (LUMO) energy of **CTN** was virtually isoenergetic with that of $[Ru(tpy)_2]^{2+}$, while the highest occupied molecular orbital (HOMO) energy of the same complex was comparable to that of $[Ru(bip)_2]^{2+}$, indicating that our initial strategy to reduce the HOMO−LUMO gap has been achieved.

Information regarding electronic excited states obtained by the time-dependent DFT (TD-DFT) method suggested that the lowest energy absorption maxima observed in the experimental absorption spectra would be best described by the mixing of multiple one-electron excitations. These electronic excitations involved the three HOMOs and three LUMOs as major platforms. Since the character of the three HOMOs and the three LUMOs are essentially metal and ligand centered in character for the former and the latter, respectively, the lowest energy absorption bands can be represented as metal-to-ligand charge transfers (MLCTs). It is important to note that an electronic excitation from HOMO to LUMO was not involved in these bands, implying that a mere reduction of the HOMO−LUMO gap cannot influence the spectral red shift directly. Better understanding about the spectral feature can be made by the TD-DFT calculation. Simulations of the electronic absorption spectra with information obtained by TD-DFT calculation reproduce the experimental counterparts successfully with 400−2000 cm^{-1} of concomitant energy shift of each constituent peak. This result suggests that DFT-based calculations play an important role in forecasting the electronic properties of ruthenium complexes.

The application of these complexes to dye-sensitized solar cells (DSSC) systems gave 0.10−0.48% of overall efficiency, which was far less than that of the N719 benchmark (6.34%). The close examination of data obtained by measuring incident photon-to-current efficiency (IPCE) values as well as $I-V$ relations indicated that the major cause of low efficiency stems from a low J_{SC} value and thus a low IPCE value. Interestingly, the IPCE value of the **CTN** system at λ_{max} was higher than that of the **TCN** system even though the experimental molar absorptivity as well as the theoretically calculated transition dipole moment of the latter exceeded those of the former. We attribute the direction of the transition dipole moment to be the key factor for this result, as in the case of N719 where strongly electron-donating isothiocyanate groups are positioned opposite to the carboxylic acid anchoring group to facilitate the electron injection toward the TiO_2 semiconductor surface. Therefore, considering this factor in the design of molecular systems might play a significant role in achieving higher efficiency solar cell systems.

Acknowledgment. This work was supported by the College of Natural Sciences, Seoul National University (305-20080071), the National Research Foundation of Korea (NRF) (2009-0093864) and the Basic Science Research Program through the NRF funded by the Ministry of Education, Science and Technology (KRF 2009-0076513 and R11-2005-065). The authors thank Dr. J.-I. Hong for use of the spectrophotometer. H.J.P. thanks the Brain Korea 21 fellowship and the Seoul Science Fellowship.

Supporting Information Available: Cyclic voltammogram of **BCN**, **TCN**, and **CTN**; SEM cross-sectional images of the fabricated TiO_2 films on the FTO layer; and the absorption spectra of dyes on DSSC system. CCDC reference number CCDC-765985 contains the supplementary crystallographic data in CIF format for this paper. This material is available free of charge via the Internet at http://pubs.acs.org.